Fabrication of a novel bifunctional material of BiOI/Ag$_3$VO$_4$ with high adsorption–photocatalysis for efficient treatment of dye wastewater

Shaomang Wang [a,b], Yuan Guan [b], Liping Wang [b], Wei Zhao [a], Huan He [a], Jun Xiao [a], Shaogui Yang [a,*], Cheng Sun [a,*]

[a] State Key Laboratory of Pollution Control and Resource Reuse, School of the Environment, Nanjing University, Nanjing 210023, PR China
[b] School of Environment and Safety Engineering, Changzhou University, Changzhou 213164, PR China

ARTICLE INFO

ABSTRACT

A novel bifunctional material with high adsorption–photocatalysis, BiOI/Ag$_3$VO$_4$ was successfully synthesized using a facile solvothermal method followed by the chemical precipitation. Among the heterogeneous materials, the 30 wt% BiOI/Ag$_3$VO$_4$ exhibited the optimal performance of adsorption-photocatalysis. The removal of 25 mg/L of basic fuchsin, malachite green and crystal violet over 30 wt% BiOI/Ag$_3$VO$_4$ was about 97%, 92% and 85%, respectively, after the adsorption for 1 h and then visible-light degradation for 2 h. The investigations of adsorption kinetics and isotherm demonstrated that the adsorption process followed the pseudo-second-order kinetic model and the Freundlich adsorption isotherm, respectively. The sequence of work function calculated by first-principles using CASTEP code was Ag < Ag$_3$VO$_4$ < BiOI, which promoted efficient separation of electron–hole pairs resulting in greatly enhanced photoactivity of BiOI/Ag$_3$VO$_4$.

© 2015 Elsevier B.V. All rights reserved.

1. Introduction

The production of synthetic dyes is increasing year by year in the world, because human beings constantly pursue color. A large amount of wastewater containing dyes is discharged without effective treatment in the process of production and use of dyes [1,2], which brings about a serious pollution to the environment and harms human health [3–5]. Current approaches of dye removal, such as traditionally biological, physical and chemical techniques, in depth degradation, cost control and harmless processing, are still far from satisfactory. Thus, the satisfied treatment of dye wastewater has been a hot topic of environment field.

In recent years, photocatalytic technique applied in the treatment of dye wastewater has attracted great research interest owning to the utilization of permanent solar energy without secondary pollution. Many photocatalysts such as TiO$_2$ [6,7], ZnO [8,9], BiVO$_4$ [10,11], Bi$_2$WO$_6$ [12,13] and Ag$_3$PO$_4$ [14,15] etc., were successfully prepared and exhibited some photoactivity for dye degradation. Current studies have shown that the photoactivity of single photocatalyst remains low. To further boost the photoactivity of catalysts, researchers developed many heterogeneous photocatalytic materials such as ZnO/g–C$_3$N$_4$ [16], TiO$_2$/graphene [17], Ag$_3$PO$_4$/graphene oxide[18], Ag$_3$PO$_4$/graphene [19], BiOCl$_x$Br$_{1-x}$ [20], Ag$_3$PO$_4$/TiO$_2$/Fe$_3$O$_4$ [21] and TiO$_2$/Ag$_3$PO$_4$/graphene [22] etc. A semiconductor Ag$_3$VO$_4$ reported by Konta et al. displayed some visible-light catalytic activity for water splitting into H$_2$ and O$_2$ [23]. The photoactivity of Ag$_3$VO$_4$ was enhanced by coupling with AgBr/Ag [24], TiO$_2$/graphene [25] and g-C$_3$N$_4$ [26]. Although degradation efficiency of pollutants was increased using Ag$_3$VO$_4$-based heterogeneous material, the material is insufficient to treat wastewater with highly concentrated pollutants. In fact, this is a common problem faced by photocatalytic degradation of contaminants, which greatly limits practical application of this technique. Increasing specific surface area of photocatalyst is an effective method to improve its performance of adsorption–photocatalysis for efficient removal of contaminants. Recently, BiOI with a narrow band gap of about 1.86 eV has become an attractive material since Huang et al. first reported that it possessed some photoactivity for degradation of methyl orange [27]. In particular, Wu and Zhang reported that BiOI had highly adsorptive capacity besides possessing some photoactivity [28,29], which was also confirmed by our recent study [30].

According to the above surveys, the combination of BiOI and Ag$_3$VO$_4$ might produce a promising material with high adsorption–photocatalysis bi-function. The aim of this work

---

* Corresponding authors. Tel.: +86 25 89680258; fax: +86 25 89680580.
E-mail addresses: yangsg@nju.edu.cn (S. Yang), envidean@nju.edu.cn (C. Sun).

is to design and prepare a bifunctional material of high adsorption–photocatalysis for efficient treatment of dye wastewater. Typical triphenylmethane dye, basic fuchsin (BF), malachite green (MG) and crystal violet (CV) are employed as target pollutants to evaluate adsorption–photocatalysis performance of the material. The removal mechanism of the dyes will be discussed in detail.

2. Experiment

2.1. Preparation of $BiOI/Ag_3VO_4$ hybrid materials

All starting materials (analytical purity) in the experiment were purchased commercially and used without further purification.

BiOI was prepared by a conventional solvothermal method in autocleave. In a typical synthesis, 2.43 g of $Bi(NO_3)_3\cdot5H_2O$ was dissolved in 40 mL of glycol, which was drop-wisely added into the same volume of (0.83 g) KI dissolved in glycol. Then, the mixture was vigorously stirred at room temperature for 1 h and was transferred to a teflon-lined autoclave (100 mL) at 160 °C for 12 h. The autoclave was naturally cooled to room temperature. The solid product was washed by deionized water and then dried at 80 °C to obtain pure BiOI.

$BiOI/Ag_3VO_4$ was prepared as follows: 0.15 g of BiOI was well dispersed in 20 mL of aqueous solution containing 1.37 g of $Na_3VO_4\cdot12H_2O$. Subsequently, 20 mL of (1.74 g) $AgNO_3$ was added drop-wisely to the above solution and then reacted to the mixture by magnetic stirring for 4 h in the dark. Finally, the resulting precipitate was washed by deionized water and dried at 80 °C to obtain 10 wt% $BiOI/Ag_3VO_4$. Other $BiOI/Ag_3VO_4$ hybrid materials with different BiOI content were fabricated by the similar method.

2.2. Characterization

XRD measurements were carried out through a diffractometer using Cu Kα radiation (Model, Shimadzu LabX XRD-6000). Fourier transform infrared spectroscopy (FT-IR) spectra were obtained via NEXUS870 (NICOLET, USA). The scanning electron microscope graphs were obtained by a SUPRA55 FSEM microscope (ZEISS, Germany). Transmission electron microscope images were collected from JEM-200CX (JEOL, Japan). X-ray photo-electron spectroscopy (XPS) measurements were performed on a PHI5000 Versa Probe electron spectrometer using Al Kα radiation (ULVAC-PHI, Japan) to identify the chemical composition and chemical state of the samples. The UV–vis diffuse reflectance spectra (DRS) were recorded by a spectrophotometer (Shimadzu UV2550) with $BaSO_4$-coated integrating sphere in the wavelength range of 200–700 nm. The photoluminescence (PL) spectra of as-fabricated materials were collected through Fluoromax-4 (HORIBA, USA) with an excitation wavelength at 350 nm. BET specific areas of the samples were determined using a nitrogen adsorption apparatus (Micromeritics ASAP 2010 instrument).

2.3. Adsorption and photocatalytic reaction

The performance of adsorption–photocatalysis of as-fabricated samples was evaluated by removing basic fuchsin (BF), malachite green (MG) and crystal violet (CV) under visible-light irradiation in a photoreaction apparatus. A 500 W Xe lamp with a 420 nm cut-off filter was utilized to generate visible light of 420 nm < λ < 700 nm. For adsorption and photocatalytic reaction, 0.05 g of as-prepared sample was put into 50 mL (25 mg/L) dye solution. Prior to irradiation, the suspension was magnetically stirred for 1 h to reach adsorption–desorption equilibrium in the dark. At given time interval of visible-light irradiation, about 3 mL aliquot was collected and centrifuged to remove catalyst particle for analysis. The con-

centration of the dye was measured by UV–vis spectroscopy at its maximum absorption wavelength.

2.4. Photoelectrochemical measurement

Photocurrent was measured on an electrochemical analyzer (CHI660B Instrument) in a standard three-electrode system using as-synthesized samples as the working electrodes. A platinum wire and a saturated calomel electrode were used as counter electrode and reference electrode, respectively. A 500 W Xe lamp through a 420 nm cut-off filter served as the visible-light source. Na_2SO_4 (1 mol/L) aqueous solution was utilized as the electrolyte. Working electrode was prepared as follows: 0.5 mL of sample slurry (0.5 g/mL) was dropped onto a F-doped SnO_2-coated glass (2 cm × 1.5 cm), which was dried at 120 °C for 5 h.

2.5. The determination of point of zero charge pH

The point of zero charge pH (pH_{PZC}) is the pH value of solution when the net charge on the surface of a sample is zero. The pH drift method was used to determine the pH_{PZC} [31]. First, the 11 aliquots of $NaNO_3$ (50 mL, 0.01 mol/L) solution were prepared in different flasks. Then, their pH values incremented by 1 were adjusted from 2 to 12 using 0.01 mol/L HNO_3 or NaOH. Next, 0.1 g of the sample was added to each flask and it was shaken for 24 h. Finally, the final pH was measured by pH meter (PHS-25). The pH_{PZC} is the point where the curve of pH_{final} vs $pH_{initial}$ intersects a straight line of $pH_{initial} = pH_{final}$.

2.6. Calculation methods

The generalized gradient approximation (GGA) with the Perdew–Burke–Ernzerh (PBE) correction was applied to calculate the work function based on first-principles using CASTEP code. The K point in the Brilliouin Zone was set to $6 \times 6 \times 6$. An energy cut-off of 370 eV was used for the expansion of the wave function into plane wave. The convergence threshold of geometric optimization was set at 2.0×10^{-5} eV/atom for total energy, 0.05 eV/Å for maximum force, 0.1 Gpa for pressure and 2.0×10^{-3} Å for maximum displacement. The self-consistent convergence accuracy was 2.0×10^{-6} eV/atom.
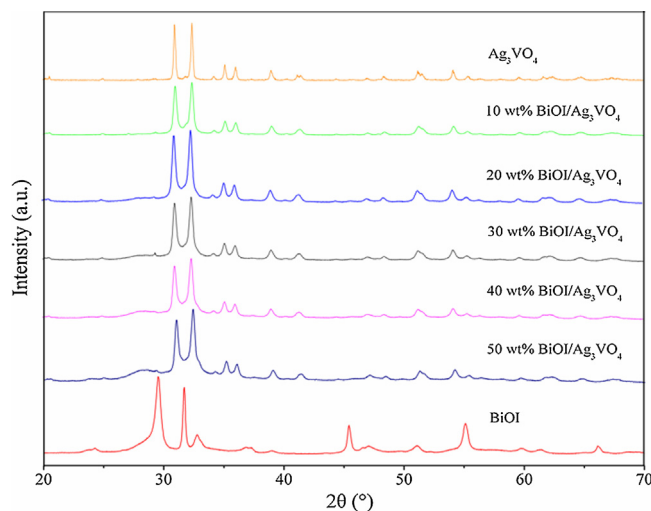

Fig. 1. XRD patterns of BiOI, Ag_3VO_4 and $BiOI/Ag_3VO_4$ composites.

3. Results and discussion

3.1. Characterization

The XRD patterns of as-synthesized samples are presented in Fig. 1. The diffraction peaks of Ag_3VO_4 can be clearly indexed as the monoclinic phase (JCPDS No. 43-0542). The crystal structure of BiOI matches well with its tetragonal phase (JCPDS No. 10-0445). The strongest peak of BiOI at about 29° corresponding to the (0 1 2) crystal plane is found to shift toward a lower 2θ value after hybridization with Ag_3VO_4. Moreover, with increasing BiOI content, the peak is more obviously observed. In addition, for the $BiOI/Ag_3VO_4$, the intensity of peak at 31° gradually weakens, and that of peak at 32° increases by degrees due to the increase of BiOI content. The results verify co-existence of BiOI and Ag_3VO_4 in $BiOI/Ag_3VO_4$ hybrid materials.

The SEM images of BiOI, Ag_3VO_4 and 30 wt% $BiOI/Ag_3VO_4$ is shown in Fig. 2a–c. Pure BiOI is a flower-like microsphere with an average diameter of 1–3 μm. Single Ag_3VO_4 displays a pebble-like shape with a diameter of 50–200 nm. From Fig. 2c, it can be seen that the BiOI and Ag_3VO_4 nicely anchor together. The lattice interlinear spacing of 0.20 and 0.19 nm corresponds to the (2 0 0) crystal plane
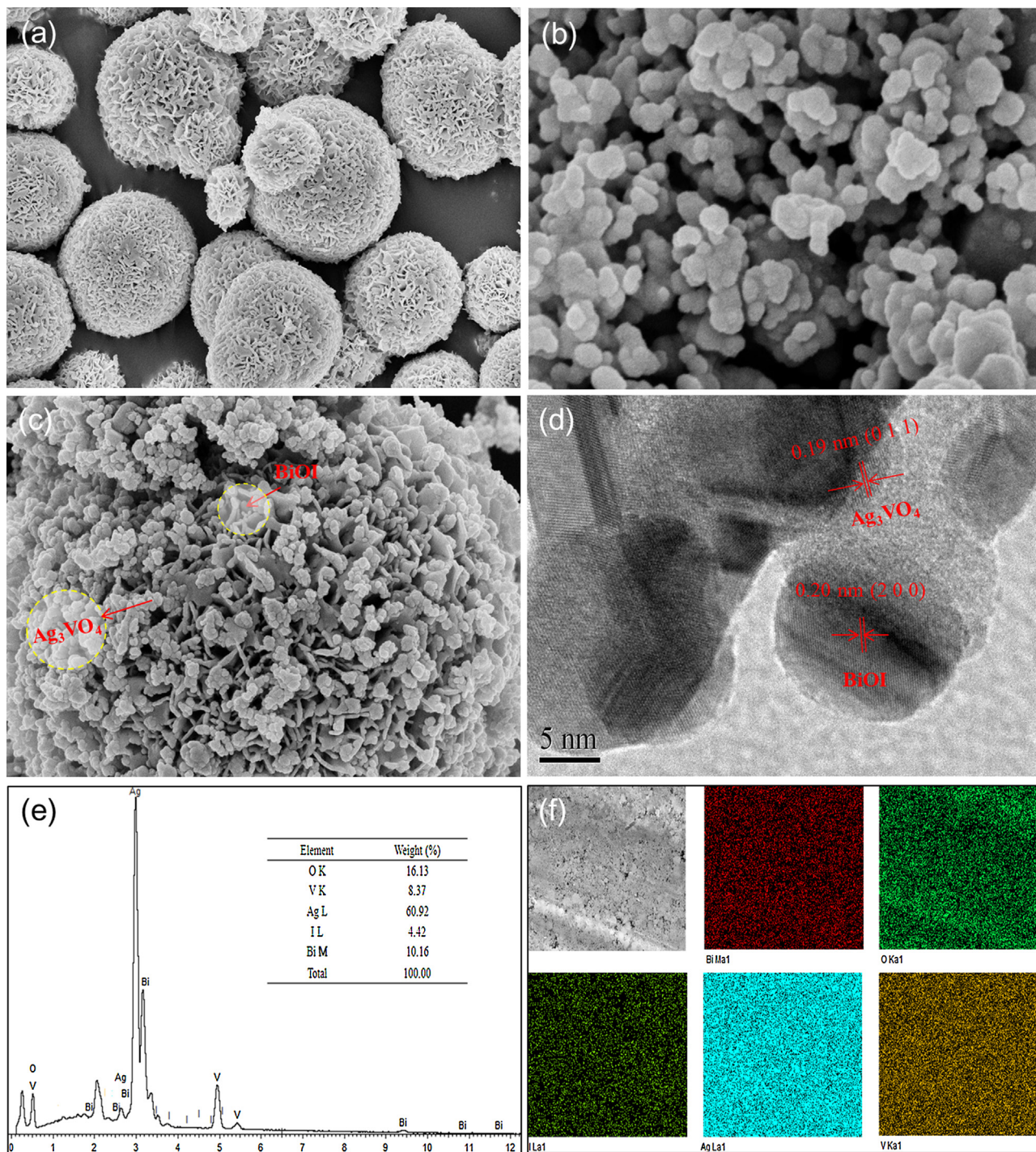

Fig. 2. SEM images of BiOI (a) and Ag_3VO_4 (b). SEM image (c), TEM image (d) and EDS (e) of 30 wt% $BiOI/Ag_3VO_4$. (f) Mappings of Bi, O, I, Ag and V.
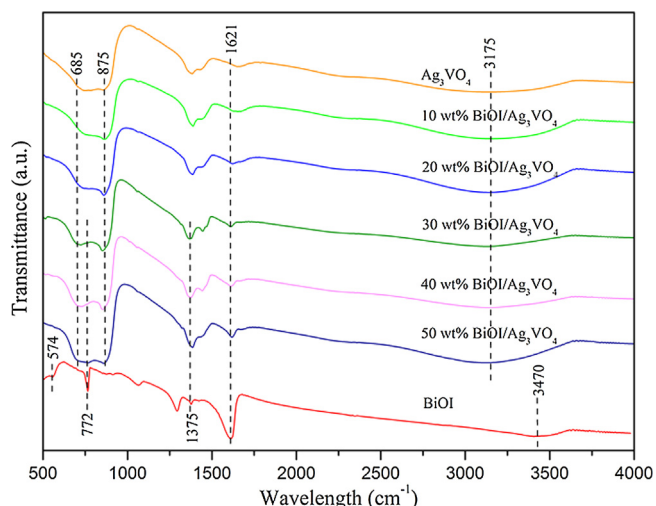
Element	Weight (%)
O K	16.13
V K	8.37
Ag L	60.92
I L	4.42
Bi M	10.16
Total	100.00

Fig. 3. FT-IR spectra of BiOI, Ag$_3$VO$_4$ and BiOI/Ag$_3$VO$_4$ hybrid materials.

of BiOI and (0 1 1) crystal plane of Ag$_3$VO$_4$ (Fig. 2d), which reveals the formation of intimate interfaces between BiOI and Ag$_3$VO$_4$ in the heterojunction. The result of EDS analysis (Fig. 2e and f) is in accord with the elements of 30 wt% BiOI/Ag$_3$VO$_4$.

Fig. 3 illustrates the FT-IR spectra of as-fabricated samples. The peaks at 685 and 875 cm^{-1} for pure Ag$_3$VO$_4$ are assigned to the symmetry stretching vibration of V—O—V units and V=O double bond vibration, respectively [32]. For pure BiOI, a peak at 574 cm^{-1} belongs to symmetrical A$_2$u-type vibration of the Bi—O bond [33,34]. The absorption at 772 cm^{-1} originates from asymmetrical stretching vibration of the Bi—O bond [35]. The characteristic peaks of BiOI at 772 and 1375 cm^{-1} are obviously present in BiOI/Ag$_3$VO$_4$ with the increase of BiOI content. In addition, the presence of the sharp and strong absorption at 1621 cm^{-1} and a broad peak at 3 1 7 5–3 4 7 0 cm^{-1} are ascribed to the δ(O—H) bending vibration and ν(O—H) stretching vibration, respectively, owing to the adsorption of free water molecule on the material surface [36]. The analyses of FT-IR further indicate that the BiOI is successfully incorporated in BiOI/Ag$_3$VO$_4$.

The elemental composition and chemical state of as-synthesized samples are examined by XPS. The survey scan spectra displays Bi 4f, I 3d, Ag 3d, V 2p and O 1s peaks (Fig. 4a), which is consistent with the chemical composition of BiOI, Ag$_3$VO$_4$ and 30 wt% BiOI/Ag$_3$VO$_4$. The peaks of Bi 4f$_{7/2}$ and Bi 4f$_{5/2}$ are observed at 158.2 and 163.7 eV, respectively (Fig. 4b), which belong to the characteristic of Bi^{3+} ions in BiOI [37,38]. The peaks of Bi 4f$_{7/2}$ and Bi 4f$_{5/2}$ for 30 wt% BiOI/Ag$_3$VO$_4$ at 158.3 and 163.8 eV are higher than those of pure BiOI. A similar shift is also found in the XPS spectra of I 3d, Ag 3d and V 2p, respectively (Fig. 4c–e). Additionally, the O1s spectra of single Ag$_3$VO$_4$ locates at 528.7 eV, which shifts toward a higher energy of 529.1 eV after hybridization with BiOI (Fig. 4f). The peaks of O 1s at 529.4 and 530.8 eV are attributed to Bi—O and I—O bonds in pure BiOI [39,40], which move to 529.7 and 532.1 eV after the formation of BiOI/Ag$_3$VO$_4$. Such inner shift of the orbits originates from the interaction of BiOI with Ag$_3$VO$_4$. The analyses distinctly reveal that the interaction between BiOI and Ag$_3$VO$_4$ is chemical bonding rather than a simple physical mixing.

The specific surface area and porosity property of as-prepared samples are revealed in Fig. 5 and Fig. S1. The isotherms of the samples with a distinct hysteresis loop are characteristic of IV type, suggesting that the as-synthesized samples belong to meso-porous materials. The surface area and pore diameter of these samples are shown in Table S1. The BET specific surface area of BiOI and Ag$_3$VO$_4$ are about 36.5 and 2.3 m^2/g, respectively, whereas those of the heterogeneous materials are increased from 6.9 to 13.7 m^2/g

with the increase of BiOI content. The pore diameter of BiOI and Ag$_3$VO$_4$ determined are 18.7 and 9.2 nm, while those are increased from 10.8 to 13.5 nm after Ag$_3$VO$_4$ hybridized by BiOI. The results show that the adsorption capacity of Ag$_3$VO$_4$ can be improved after hybridization with BiOI.

The optical properties of BiOI, Ag$_3$VO$_4$ and BiOI/Ag$_3$VO$_4$ are depicted in Fig. 6. Pure BiOI displays strong photo-absorption from the UV light to visible light shorter than 660 nm, and its band-gap energy revealed in the inset is approximately 1.86 eV. Bare Ag$_3$VO$_4$ can absorb solar energy with a wavelength shorter than 574 nm, and its band-gap energy is about 2.2 eV. With the increase of BiOI content, the absorbance edges of BiOI/Ag$_3$VO$_4$ present a gradual red shift compared to pure Ag$_3$VO$_4$. The results from DSR imply that the photocatalysts should possess visible-light photoactivity.

3.2. Performance of adsorption–photocatalysis of BiOI/Ag$_3$VO$_4$

The performance of adsorption–photocatalysis of as-fabricated samples is tested by measuring removal of BF from wastewater. Adsorption is pre-carried out in the dark for 1 h and then degradation proceeded at t = 0. Fig. 7 depicts the removal of BF adsorbed and catalyzed by BiOI, Ag$_3$VO$_4$ and BiOI/Ag$_3$VO$_4$, respectively. It is observed that the adsorption capacity of pure BiOI and BiOI/Ag$_3$VO$_4$ hybrid materials is obviously stronger than that of single Ag$_3$VO$_4$. After the adsorption for 1 h, more than 40% of BF is eliminated by BiOI and BiOI/Ag$_3$VO$_4$, while only 6% of BF is adsorbed through Ag$_3$VO$_4$. For the photodegradation, the absorbance of BF solution dose not decrease without photocatalyst under visible-light irradiation for 2 h, indicating that BF is stable and is difficult to be photolysis. Compared to single BiOI and Ag$_3$VO$_4$, the as-synthesized BiOI/Ag$_3$VO$_4$ can effectively decompose BF under visible-light illumination. More than 40% of BF from the dye solution is degraded using BiOI/Ag$_3$VO$_4$ after visible-light irradiation for 2 h, while only 19% and 16% of BF degradation are achieved by pure Ag$_3$VO$_4$ and BiOI. After the adsorption for 1 h and then visible-light degradation for 2 h, single Ag$_3$VO$_4$ and BiOI can remove about 25% and 65% of BF, respectively, while more than 80% of BF can be eliminated by BiOI/Ag$_3$VO$_4$. The highest removal, 97% of BF, is achieved by 30 wt% BiOI/Ag$_3$VO$_4$.

Another two typical triphenylmethane dye of MG and CV are chosen as target pollutants to further test the performance of adsorption–photocatalysis of 30 wt% BiOI/Ag$_3$VO$_4$. From Fig. S2, the hybrid material exhibits excellent ability for MG and CV removal. About 92% of MG and 85% of CV are eliminated after 1 h of adsorption and photodegradation for 2 h, respectively.

The stability of the bi-functional material is very important for practical application. The transformation of Ag$^+$ into Ag^0 often happens in some Ag$^+$-containing semiconductors [41], which might decrease removal of pollutants. A small amount of silver is generated after three recycling runs of 30 wt% BiOI/Ag$_3$VO$_4$ (Fig. S3). To our surprise, the 30 wt% BiOI/Ag–Ag$_3$VO$_4$ still maintains high photoactivity for BF, MG and CV degradation, respectively (Fig. S4), which might be ascribed to plasmon-resonance effect of Ag [24].

3.3. Adsorption kinetics and isotherms of adsorption

The adsorption kinetics of BF, MG and CV on 30 wt% BiOI/Ag$_3$VO$_4$ is shown in Fig. 8. The adsorption capacity of BF, MG and CV increases firstly and then remains unchanged with time (Fig. 8a). The adsorption equilibrium is achieved after about 15 min.

In order to investigate adsorption behavior, the experimental data of adsorption are tested by pseudo-first-order equation and pseudo-second-order equation, respectively. Two adsorption kinetic equations are expressed as follows [42]:
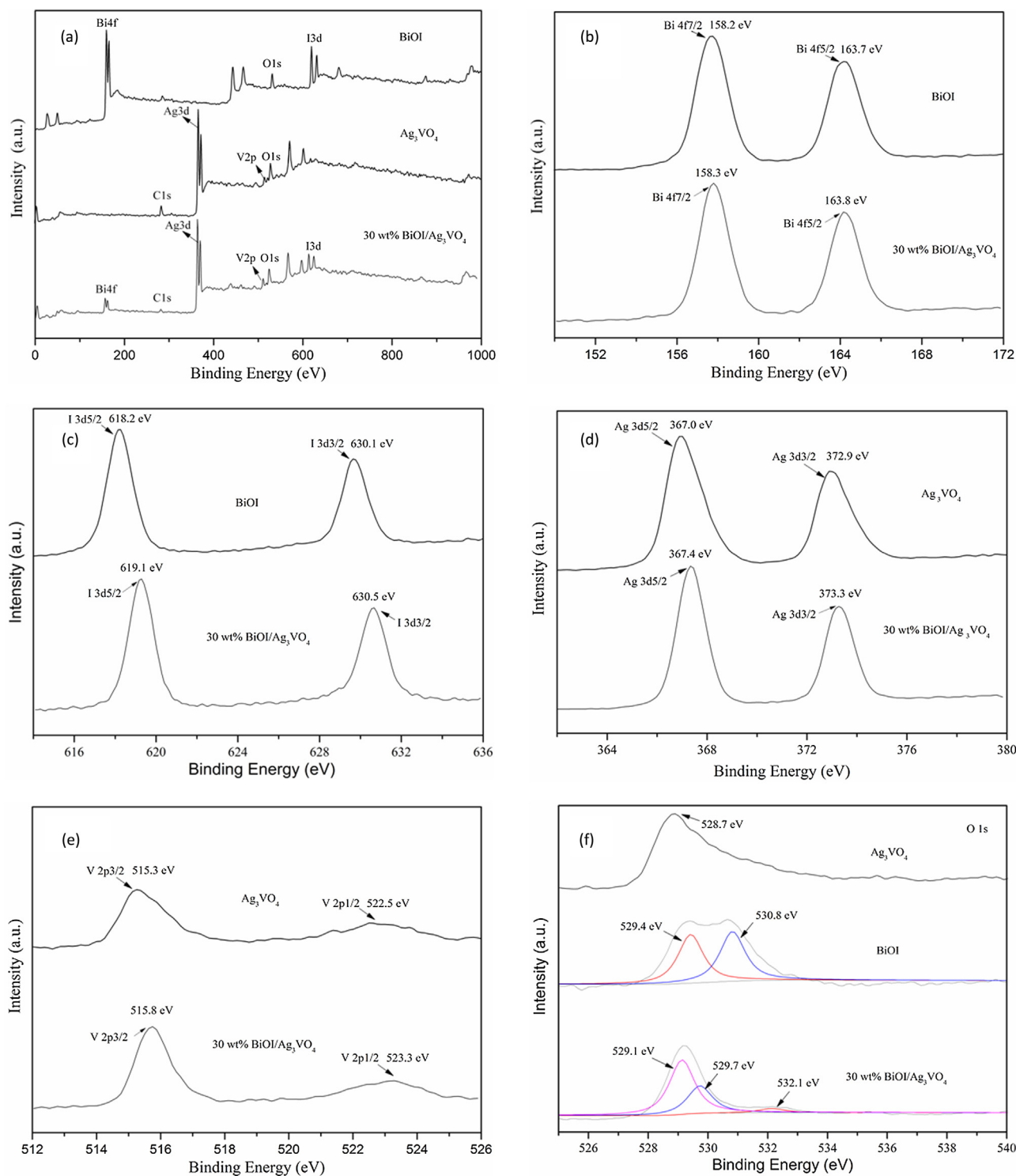
$$\ln(q_e - q_t) = \ln q_e - k_1 t \tag{1}$$

Fig. 4. XPS spectra: (a) the survey scan of the samples; (b) Bi 4f and (c) I 3 d of BiOI and 30 wt% BiOI/Ag$_3$VO$_4$; (d) Ag 3 d and (e) V 2p of Ag$_3$VO$_4$ and 30 wt% BiOI/Ag$_3$VO$_4$; (f) O 1s of BiOI, Ag$_3$VO$_4$ and 30 wt% BiOI/Ag$_3$VO$_4$.

$$\frac{t}{q_t} = \frac{1}{k_2 q_e} + \frac{t}{q_e} \tag{2}$$

where q_e and q_t represent the amount of dye adsorbed at equilibrium and at a specific time (mg/g). K_1 (min^{-1}) is the pseudo-first-order rate constant. K_2 (min^{-1}) is the pseudo-second-order rate constant.

By comparing the correlation coefficient (Table 1), it is found that the fitting results using pseudo-second-order kinetic model

are distinctly better than those of pseudo first-order kinetic model. The calculated q_e values by pseudo-second-order kinetic model are in accord with the experimental data. Thus, it can be concluded that the adsorption behavior follows pseudo-second-order kinetic model (Fig. 8b).

The adsorption isotherm is also an effective method of investigating the adsorption ability of adsorbent and understanding the interactions between the adsorbate and adsorbent. The Langmuir and Freundlich adsorption model are often selected to describe the

Table 1
Parameters of the two kinetic models of MG, BF and CV adsorption on 30 wt% BiOI/Ag$_3$VO$_4$ at 25 °C.

| Dyes	Pseudo-first-order equation			Pseudo-second-order equation		
25 (mg/L)	K_1 (1/min)	q_e (mg/g)	R^2	K_2 (g/mg·min)	q_e (mg/g)	R^2
BF	0.0452	2.6	0.3469	1.0325	11.8	0.9968
CV	0.105	5.3	0.5476	0.9464	12.7	0.9998
MG	0.0986	7.1	0.5528	1.0878	15.5	0.9987
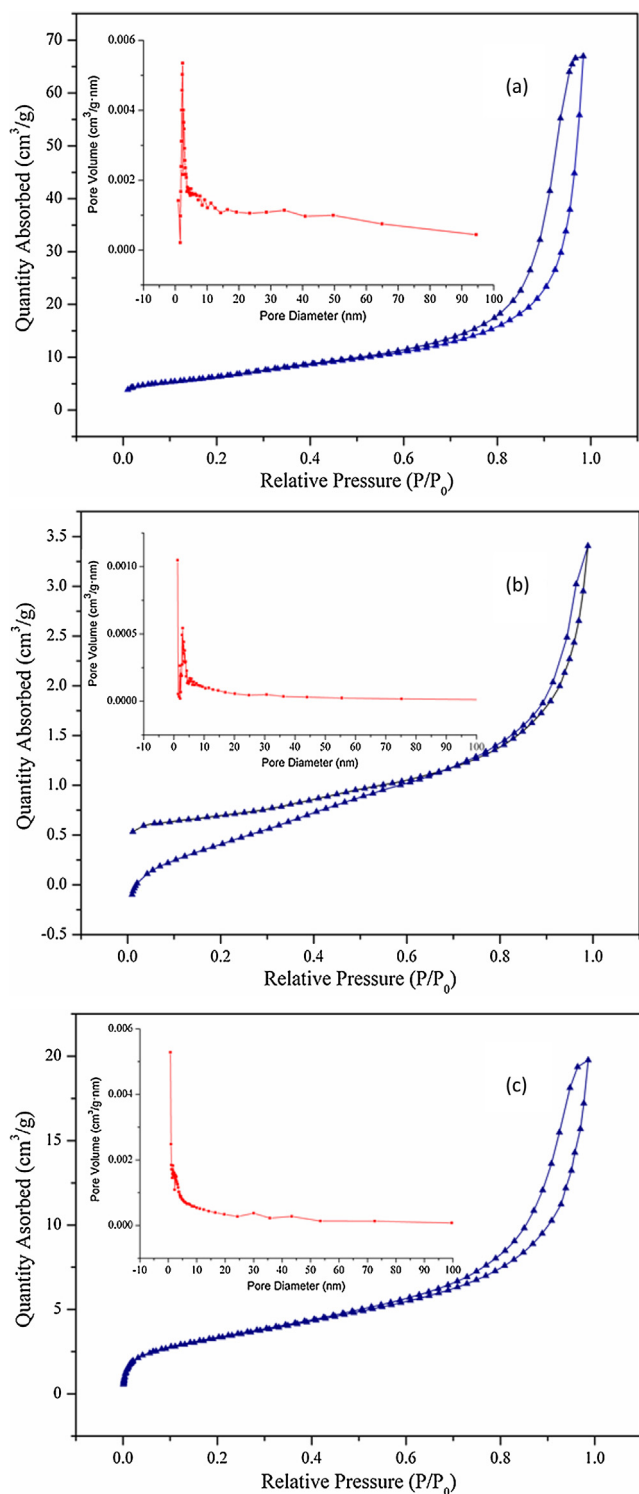
Fig. 5. Nitrogen adsorption–desorption isotherm and pore-size distribution (inset) for (a) BiOI, (b) Ag$_3$VO$_4$ and (c) 30 wt% BiOI/Ag$_3$VO$_4$.
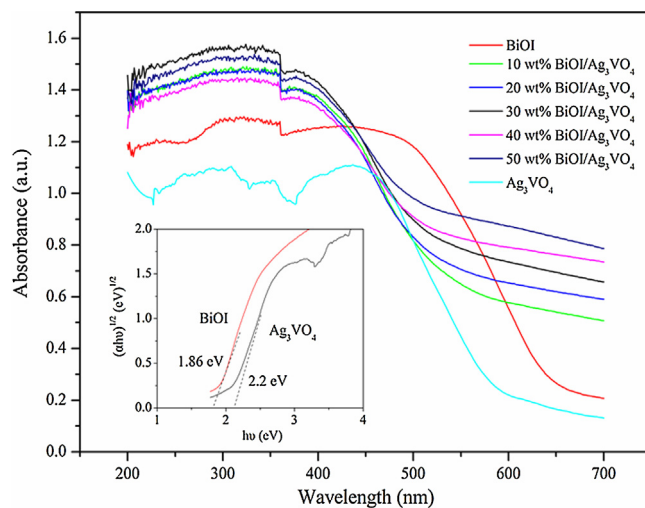
Fig. 6. UV–vis diffuse reflectance spectra of BiOI, Ag$_3$VO$_4$ and BiOI/Ag$_3$VO$_4$ composites.

sorption phenomenon of the sorbents. Their models are given as follows [43,44]:

$$q_e = \frac{bq_mC_e}{1 + bC_e} \qquad (3)$$

$$q_e = KC_e^n \qquad (4)$$

where b (L/mg) and q_m are the constant of adsorption intensity and the adsorption capacity of theoretical maximum, respectively. C_e (mg/L) is the concentration of equilibrium adsorption in the solution. K (mg^{1-n} L^n/g) and n ($0 < n < 1$) are the Freundlich constants describing the adsorption capacity and linearity index, respectively.
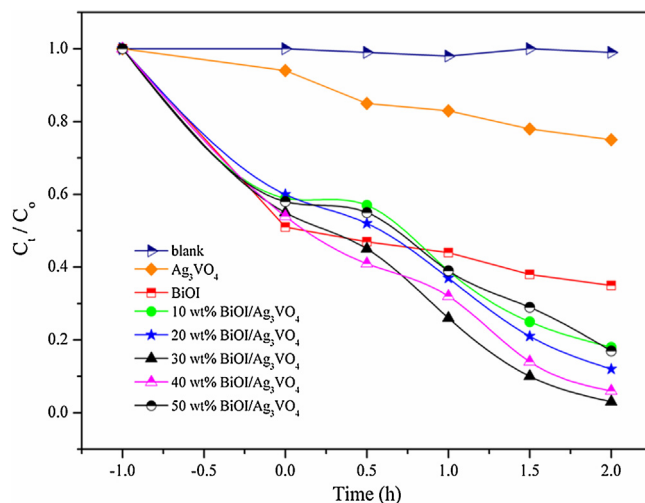
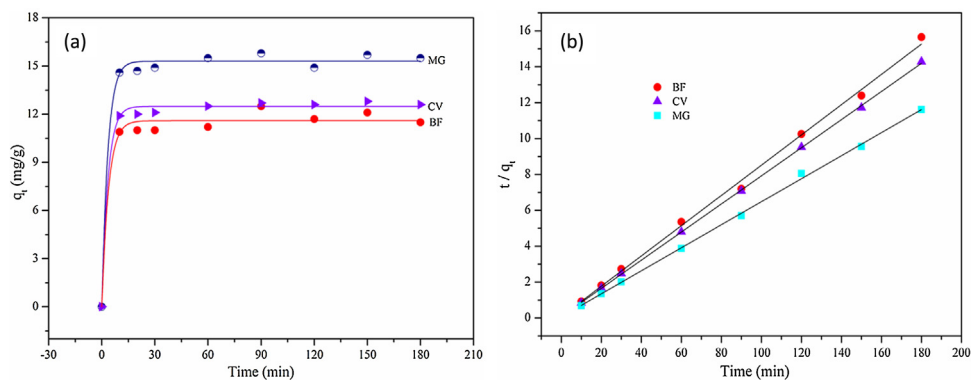**Fig. 7.** The removal of BF by as-prepared samples as a function of time.

Fig. 8. (a) The adsorption-kinetics curve and (b) Pseudo-second-order kinetics of MG, BF and CV adsorption on 30 wt% BiOI/Ag$_3$VO$_4$ at 25 °C.
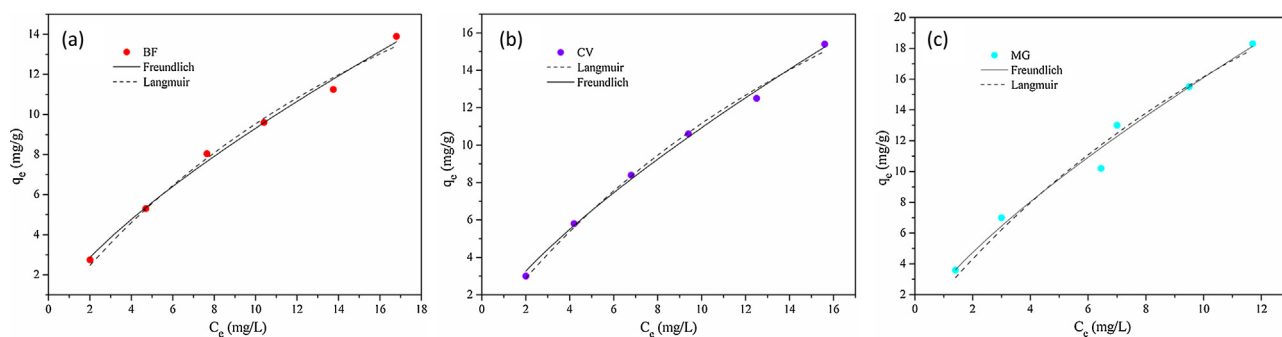

Fig. 9. (a) MG, (b) BF and (c) CV adsorption on 30 wt% BiOI/Ag$_3$VO$_4$ fitted by Langmuir and Freundlich isotherms at 25 °C, respectively.

Fig. 9a–c illustrate adsorption isotherm of MG, BF and CV on over 30 wt % BiOI/Ag$_3$VO$_4$ at 25 °C. Compared with fitting correlation coefficient (Table 2), the results fitted by Freundlich model are better than those of Langmuir model, implying that the adsorption belongs to multilayer adsorption.

3.4. Absorption mechanism

The pH value of dye solution strongly influences the surface-charge property of 30 wt% BiOI/Ag$_3$VO$_4$, which directly affects adsorption behavior of MG, BF and CV on the bifunctional material.
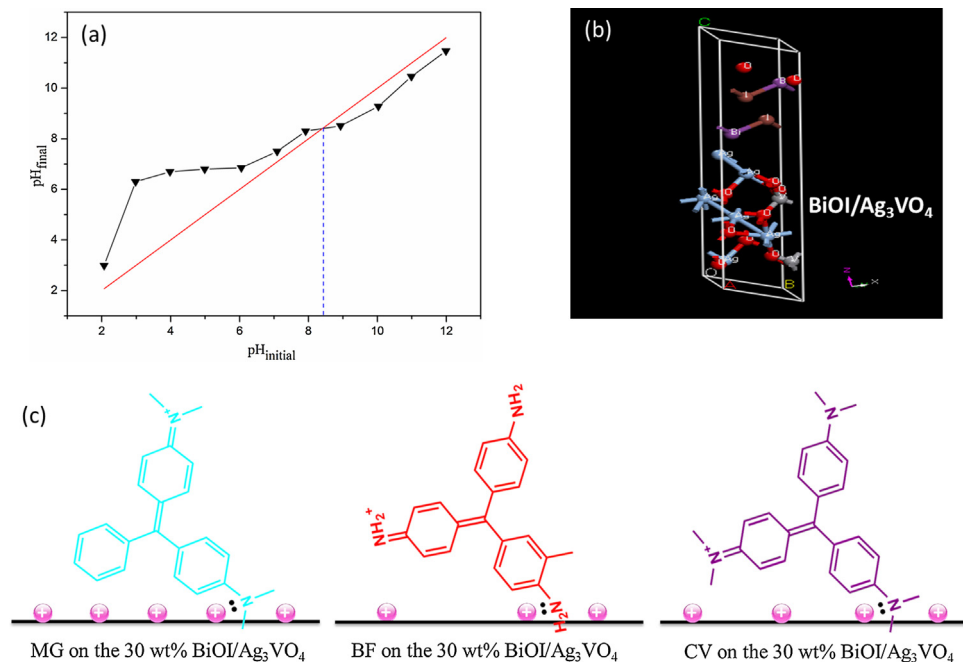

Fig. 10. (a) Point of zero charge of 30 wt% BiOI/Ag$_3$VO$_4$. (b) The crystal structure of BiOI/Ag$_3$VO$_4$. (c) Schematic diagram of supposed adsorption mode of MG, BF and CV molecules on the surface of 30 wt% BiOI/Ag$_3$VO$_4$ under the experimental conditions.

Table 2
The constants of Langmuir and Freundlich isotherms for MG, BF and CV adsorption over 30 wt% BiOI/Ag$_3$VO$_4$ at 25 °C.

Dyes	Langmuir model			Freundlich model		
25(mg/L)	q_m (mg/g)	b (L/mg)	R^2	K (mg^{1-n}L^n/g)	n	R^2
BF	33.45	0.0399	0.9884	1.7247	0.7326	0.9921
CV	39.27	0.0397	0.9942	1.9472	0.7491	0.9957
MG	51.19	0.0461	0.9697	2.8038	0.7591	0.9778

When the pH value of dye solution is lower than pH$_{PZC}$ of 30 wt% BiOI/Ag$_3$VO$_4$, its surface is positively charged. While the pH value of dye solution is higher than pH$_{PZC}$ of the material, its surface is negatively charged.

As shown in Fig. 10 a, the point of zero charge of 30 wt% BiOI/Ag$_3$VO$_4$ is about 8.47. The pH values of MG, BF and CV solutions determined are approximately 4.75, 6.48 and 6.02, respectively. Under the three pH conditions, the surface of 30 wt% BiOI/Ag$_3$VO$_4$ is positively charged. Because the difference sequence between pH value of dye solution and pH$_{PZC}$ of 30 wt% BiOI/Ag$_3$VO$_4$ is MG > CV > BF, the number sequence of positive charge on the surface of 30 wt% BiOI/Ag$_3$VO$_4$ is MG > CV > BF. Thus, the amount of dye adsorbed on the bifunctional material is MG > CV > BF, which is in line with the fitting results of pseudo-second-order kinetic model.

In addition, due to the electrostatic interaction, the three dyes tend to adsorb on the surface of the material by the negatively charged or electron abundant group. For MG, BF and CV molecules, the lone pair electrons of nitrogen atom are negatively charged. Meanwhile, the methyl group is electron-donating group. Therefore, the MG and CV molecules tend to adsorb on the surface of 30 wt% BiOI/Ag$_3$VO$_4$ through lone pair electrons of nitrogen atom of dimethylamino group, while the BF molecules tend to adsorb via lone pair electrons of nitrogen atom of amino group adjacent to
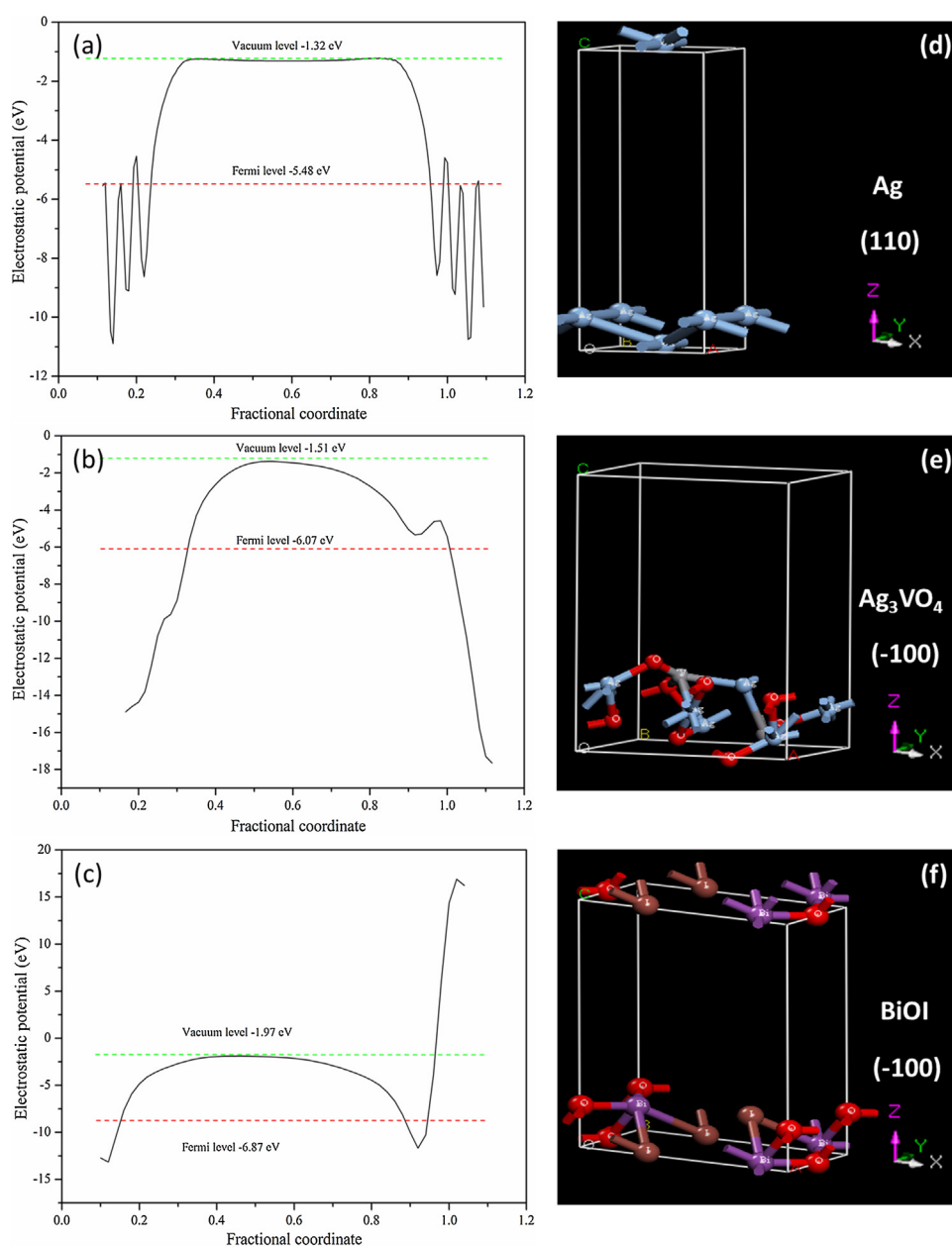

Fig. 11. (a)–(c) the work function of Ag, Ag$_3$VO$_4$ and BiOI. (d)–(f) the crystal structure of Ag (110), Ag$_3$VO$_4$ (−100) and BiOI (−100).
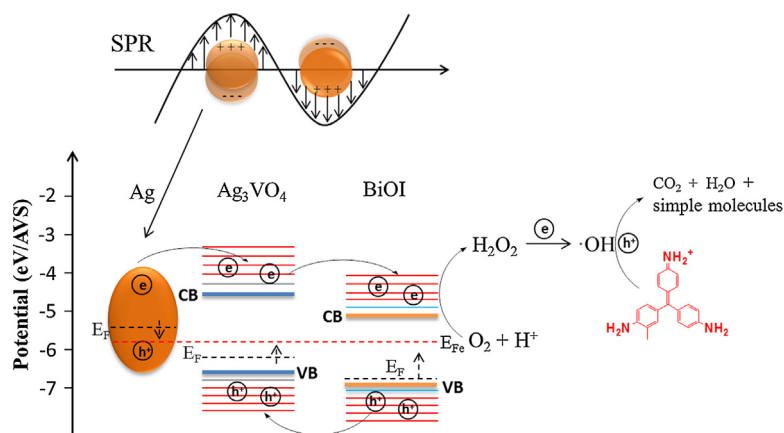
Fig. 12. Schematic diagram of the enhanced photoactivity.

methyl group. The speculation adsorption for the MG, BF and CV molecules on the surface of 30 wt% BiOI/Ag$_3$VO$_4$ under the experimental conditions is illustrated in Fig. 10c.

3.5. The mechanism of the enhanced photoactivity

3.5.1. The band-edge position of Ag$_3$VO$_4$ and BiOI

The positions of the conduction and valence band-edge of Ag$_3$VO$_4$ obtained are about 0.04 eV/NHE (−4.54 eV/AVS) and 2.24 eV/NHE (−6.74 eV/AVS) from the literature [26]. For the BiOI, the positions of the conduction and valence band-edge are approximately 0.56 eV/NHE (−5.06 eV/AVS) and 2.42 eV/NHE (−6.92 eV/AVS) in the light of the literature [45]. The matched positions of the conduction and valence band-edge between BiOI and Ag$_3$VO$_4$ are beneficial for efficiently separating electron–hole pairs of BiOI/Ag$_3$VO$_4$, which will improve its photoactivity [39,46].

3.5.2. The work function of Ag, Ag$_3$VO$_4$ and BiOI

Fig. 11a–c present the calculated work-function for the clean Ag, Ag$_3$VO$_4$ and BiOI by first-principles calculations using CASTEP code. The work function of 4.16 eV/AVS for the clean Ag is obtained according to calculated the vacuum level of −1.32 eV and Fermi level of −5.48 eV. The work function of Ag$_3$VO$_4$ is 4.56 eV based on the vacuum level of −1.51 eV and Fermi level of −6.07 eV. For the BiOI, the vacuum level and Fermi level locate at −1.97 eV and −6.87 eV, respectively. Thus, the work function of BiOI calculated is 4.90 eV. Because the sequence of the work function is Ag < Ag$_3$VO$_4$ < BiOI, the photo-generated electrons of Ag owing to the plasmon-resonance can easily transfer to Ag$_3$VO$_4$ [24], then to BiOI. With the transfer of electrons, the Fermi level of Ag moves

downward, while those of Ag$_3$VO$_4$ and BiOI shift upward until the equilibrium state is achieved. Finally, the recombination of photo-generated electron–hole is efficiently prevented as a result of the special electron transfer. It is well known that the efficient separation of electron–hole pairs is crucial for boosting photoactivity of photocatalysts. Thence, the photoactivity of Ag$_3$VO$_4$ is greatly promoted after it is hybridized by BiOI.

According to the above investigations, electron–hole pairs' separation in the bifunctional material under visible-light irradiation is proposed in Fig. 12.

To prove above-enhanced mechanism, photoluminescence technique is utilized to detect the recombination of electron–hole pairs in BiOI, Ag$_3$VO$_4$ and 30 wt% BiOI/Ag$_3$VO$_4$. In general, the fluorescence intensity with lower value implies less recombination of electron–hole pairs and higher photoactivity. Fig. 13a depicts that bare BiOI excited at 350 nm has a strong emission peak at about 630 nm. For pure Ag$_3$VO$_4$, the intensity of emission peak at approximately 587 nm is a little lower than that of pure BiOI. Compared to pure BiOI and Ag$_3$VO$_4$, the 30 wt% BiOI/Ag$_3$VO$_4$ exhibits obviously lower intensity of emission peak. This confirms that the combination of BiOI and Ag$_3$VO$_4$ can significantly boost separation of electron–hole pairs.

To give further evidence to support the above-suggested mechanism, the transient photocurrent value of BiOI, Ag$_3$VO$_4$ and 30 wt% BiOI/Ag$_3$VO$_4$ electrodes are recorded for several on–off cycles of irradiation. The higher photocurrent value means more efficient separation of photogenerated electron–hole pairs. As shown in Fig. 13b, the photocurrent rapidly increases as soon as the irradiation of light turns on, and then the photocurrent decreases to a constant value when the light is off, which is reproducible.
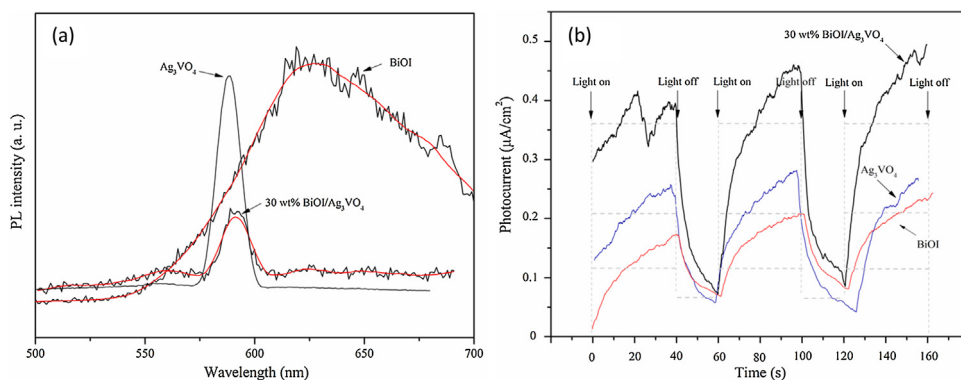

Fig. 13. (a) Photoluminescence spectra and (b) transient photocurrent of BiOI, Ag$_3$VO$_4$ and 30 wt% BiOI/Ag$_3$VO$_4$.

Compared with single Ag_3VO_4 and BiOI, the photocurrent intensity of 30 wt% $BiOI/Ag_3VO_4$ distinctly increases, which is consistent with the results of PL.

4. Conclusions

In this work, a novel bifunctional material with high adsorption–photocatalysis, $BiOI/Ag_3VO_4$ was successfully fabricated through the hybridization of BiOI and Ag_3VO_4. For the heterogeneous materials, the 30 wt% $BiOI/Ag_3VO_4$ exhibited the strongest capacity for the removal of BF, MG and CV. The reusability experiments suggested that the hybrid material possessed good stability. The measurement result of the zero charge indicated that the three dyes tended to adsorb on the surface of 30 wt% $BiOI/Ag_3VO_4$ by the lone pair electrons of nitrogen atom due to the electrostatic interaction. Since the material with adsorption–photocatalysis bi-function can efficiently remove organic pollutants, it might provide a way to design an environmental purification material.

Acknowledgments

Appendix A. Supplementary data

Supplementary data associated with this article can be found, in the online version, at http://dx.doi.org/10.1016/j.apcatb.2014.12.047.

References

[1] S. Papic, N. Koprivanac, A.L. Bozic, A. Metes, Dyes Pigm. 62 (2004) 291–298.
[2] A. Latif, S. Noor, Q.M. Sharif, M. Najeebullah, J. Chem. Soc. Pak. 32 (2010) 115–124.
[3] W. Au, S. Pathak, C.J. Collie, T.C. Hsu, Mutat. Res. 58 (1978) 269–276.
[4] S. Srivastava, R. Sinha, D. Roy, Aquat. Toxicol. 66 (2004) 319–329.
[5] T.B. Zanoni, M. Tiago, F. Faiao-Flores, S.B. de Moraes Barros, A. Bast, G. Hageman, D.P. de Oliveira, S.S. Maria-Engler, Toxicol. Lett. 227 (2014) 139–149.
[6] I.K. Konstantinou, T.A. Albanis, Appl. Catal. B 49 (2004) 1–14.
[7] X. Chen, S.S. Mao, Chem. Rev. 107 (2007) 2891–2959.
[8] S. Chakrabarti, B.K. Dutta, J. Hazard. Mater. 112 (2004) 269–278.
[9] J. Yu, X. Yu, Environ. Sci. Technol. 42 (2008) 4902–4907.
[10] N.C. Castillo, A. Heel, T. Graule, C. Pulgarin, Appl. Catal. B 95 (2010) 335–347.
[11] S. Obregon, A. Caballero, G. Colon, Appl. Catal. B 117 (2012) 59–66.
[12] A.K.P. Mann, E.M.P. Steinmiller, S.E. Skrabalak, Dalton Trans. 41 (2012) 7939–7945.
[13] H. Fu, S. Zhang, T. Xu, Y. Zhu, J. Chen, Environ. Sci. Technol. 42 (2008) 2085–2091.
[14] Z. Yi, J. Ye, N. Kikugawa, T. Kako, S. Ouyang, H. Stuart-Williams, H. Yang, J. Cao, W. Luo, Z. Li, Y. Liu, R.L. Withers, Nat. Mater. 9 (2010) 559–564.
[15] Y. Bi, H. Hu, S. Ouyang, Z. Jiao, G. Lu, J. Ye, Chem.-Eur. J. 18 (2012) 14272–14275.
[16] Y. Wang, R. Shi, J. Lin, Y. Zhu, Energ. Environ. Sci. 4 (2011) 2922–2929.
[17] X. Yang, J. Qin, Y. Li, R. Zhang, H. Tang, J. Hazard. Mater. 261 (2013) 342–350.
[18] H. Cui, X. Yang, Q. Gao, H. Liu, Y. Li, H. Tang, R. Zhang, J. Qin, X. Yan, Mater. Lett. 93 (2013) 28–31.
[19] X. Yang, H. Cui, Y. Li, J. Qin, R. Zhang, H. Tang, ACS Catal. 3 (2013) 363–369.
[20] H. Gnayem, Y. Sasson, ACS Catal. 3 (2013) 186–191.
[21] J.-W. Xu, Z.-D. Gao, K. Han, Y. Liu, Y.-Y. Song, ACS Appl. Mater. Interfaces 6 (2014) 15122–15131.
[22] X. Yang, J. Qin, Y. Jiang, R. Li, Y. Li, H. Tang, RSC Adv. 4 (2014) 18627–18636.
[23] R. Konta, H. Kato, H. Kobayashi, A. Kudo, Phys. Chem. Chem. Phys. 5 (2003) 3061–3065.
[24] Q. Zhu, W.-S. Wang, L. Lin, G.-Q. Gao, H.-L. Guo, H. Du, A.-W. Xu, J. Phys. Chem. C 117 (2013) 5894–5900.
[25] J. Wang, P. Wang, Y. Cao, J. Chen, W. Li, Y. Shao, Y. Zheng, D. Li, Appl. Catal. B 136 (2013) 94–102.
[26] S. Wang, D. Li, C. Sun, S. Yang, Y. Guan, H. He, Appl. Catal. B 144 (2014) 885–892.
[27] W. Wang, F. Huang, X. Lin, J. Yang, Catal. Commun. 9 (2008) 8–12.
[28] S. Wu, J. Fang, X. Hong, K.S. Hui, Y. Chen, Dalton Trans. 43 (2014) 2611–2619.
[29] B. Zhang, G. Ji, M.A. Gondal, Y. Liu, X. Zhang, X. Chang, N. Li, J. Nanopart. Res. 15 (2013).
[30] X. Wang, S. Yang, H. Li, W. Zhao, C. Sun, H. He, RSC Adv. 4 (2014) 42530–42537.
[31] N. Wibowo, L. Setyadhi, D. Wibowo, J. Setiawan, S. Ismadji, J. Hazard. Mater. 146 (2007) 237–242.
[32] M. Xue, J. Ge, H. Zhang, J. Shen, Appl. Catal. A-Gen. 330 (2007) 117–126.
[33] Y. Wang, K. Deng, L. Zhang, J. Phys. Chem. C 115 (2011) 14300–14308.
[34] C. Wang, C. Shao, Y. Liu, L. Zhang, Scr. Mater. 59 (2008) 332–335.
[35] Z. Liu, X. Xu, J. Fang, X. Zhu, J. Chu, B. Li, Appl. Surf. Sci. 258 (2012) 3771–3778.
[36] J. Cao, B. Xu, H. Lin, B. Luo, S. Chen, Dalton Trans. 41 (2012) 11482–11490.
[37] H. Liu, W. Cao, Y. Su, Y. Wang, X. Wang, Appl. Catal. B 111 (2012) 271–279.
[38] G. Dai, J. Yu, G. Liu, J. Phys. Chem. C 115 (2011) 7339–7346.
[39] J. Jiang, X. Zhang, P. Sun, L. Zhang, J. Phys. Chem. C 115 (2011) 20555–20564.
[40] C. Yu, J.C. Yu, C. Fan, H. Wen, S. Hu, Mater. Sci. Eng. B-Adv. 166 (2010) 213–219.
[41] W. Liu, X. Liu, Y. Fu, Q. You, R. Huang, P. Liu, Z. Li, Appl. Catal. B 123 (2012) 78–83.
[42] M.S. Chiou, H.Y. Li, Chemosphere 50 (2003) 1095–1105.
[43] I. Langmuir, J. Am. Chem. Soc. 38 (1916) 2221–2295.
[44] F. HMFZ, Phys. Chem. 57 (1906).
[45] C. Chang, L. Zhu, S. Wang, X. Chu, L. Yue, ACS Appl. Mater. Interfaces 6 (2014) 5083–5093.
[46] X. Zhang, L. Zhang, T. Xie, D. Wang, J. Phys. Chem. C 113 (2009) 7371–7378.